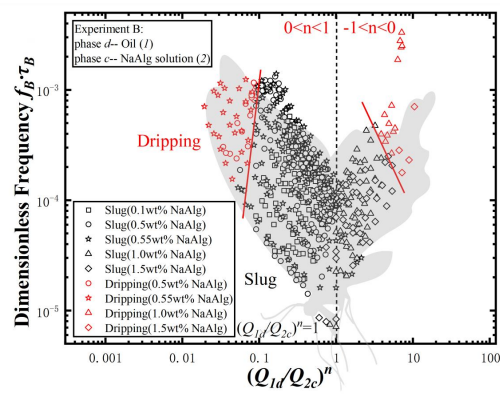
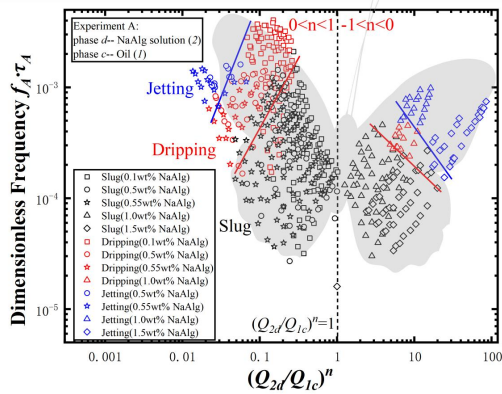
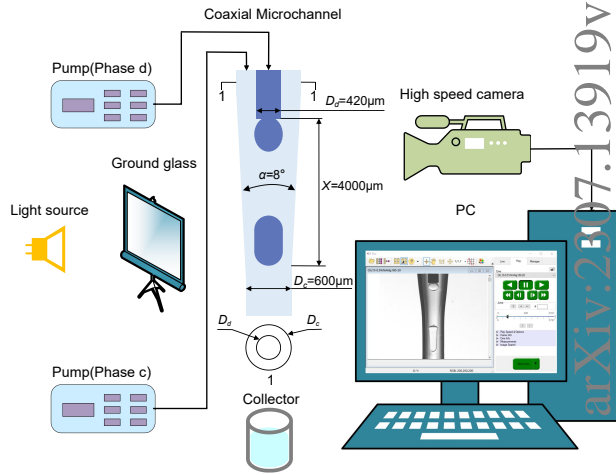


# Graphical Abstract

## Comparative Analysis of Non-Newtonian Effects on Temporal and Spatial Characteristics of Droplet Generation: Non-Newtonian Fluid as Dispersed or Continuous Phase in Coaxial Two-Phase Flow

Jinsong Zhang, Hanhua Song, Z. L. Wang



## Highlights

### **Comparative Analysis of Non-Newtonian Effects on Temporal and Spatial Characteristics of Droplet Generation: Non-Newtonian Fluid as Dispersed or Continuous Phase in Coaxial Two-Phase Flow**

Jinsong Zhang, Hanhua Song, Z. L. Wang

- Investigated temporal&spatial behaviors when interchanging of two phases.
- Modified Carreau model to find non-Newtonian index  $n < 0$ , rarely reported, exist.
- Found *Butterfly* and *Grape* distributions of separable phase charts, only when introducing of  $n$ .
- Discovered temporal&spatial synchronous transition phenomenon.

# Comparative Analysis of Non-Newtonian Effects on Temporal and Spatial Characteristics of Droplet Generation: Non-Newtonian Fluid as Dispersed or Continuous Phase in Coaxial Two-Phase Flow

Jinsong Zhang<sup>a</sup>, Hanhua Song<sup>a</sup> and Z. L. Wang<sup>b,\*</sup>

<sup>a</sup>School of Mechatronic Engineering and Automation, Shanghai University, No.149 Yanchang Road, Shanghai, 200072, P. R. China

<sup>b</sup>Shanghai Key Laboratory of Mechanics in Energy Engineering, Shanghai Institute of Applied Mathematics and Mechanics, School of Mechanics and Engineering Science, Shanghai University, Shanghai, 200444, P. R. China

## ARTICLE INFO

### Keywords:

non-Newtonian fluid  
microfluidics  
two-phase flows  
coaxial flow  
Carreau model  
monodisperse droplet

## ABSTRACT

Comparative Analysis on temporal and spatial behaviors of droplets produced in a converging co-flow has been investigated when interchanging of phases, NaAlg (non-Newtonian) and soybean oil (Newtonian). The Carreau model is promoted and gave rarely reported negative non-Newtonian index,  $n < 0$ , by which phase diagrams of "butterfly distribution" on temporal  $f \cdot \tau \sim (Q_d/Q_c)^n$  space and "grape distribution" on spatial  $d^*/D_c \sim (Q_d/Q_c)^n$  space are distinguished for the first time. These flow charts shows symmetry on refined expression  $(Q_d/Q_c)^n = 1$ , (either  $Q_d/Q_c = 1$  or  $n = 0$ ) for both comparative experiments. We also find an interesting synchronous transition phenomenon exist, where the interchanging of disperse and continuous phases will not affect their temporal and spatial characteristics of drop generating, which is dynamically rarely happened.

## 1. Introduction

Microfluidics [1–3] pertains to the application of scientific and technological principles to control and manipulate micro digital fluids—ranging from picoliters to nanoliters—via microscale channels, spanning from immunoassay [4] and bioanalysis [5] to fluidic optics [6], and beyond.

A crucial research subfield within microfluidics is liquid-liquid two-phase flow [7, 8]. Techniques using two-phase flow for droplet generation in microchannels are widely used in diverse arenas, such as drug delivery [9], cell encapsulation [10], protein crystallization [11], and polymer microcapsules [12].

Typically, the microdevices for two-phase flow include cross-flowing devices (such as T-shaped [13, 14] and Y-shaped [15, 16] junctions), co-flowing devices [17, 18] (such as the converging coaxial microchannel in this study [19, 20]), and flow focusing devices [21, 22] (such as cross-shaped and coaxial junctions). Microfluidic devices are commonly fabricated from materials like polydimethylsiloxane (PDMS), quartz glass, and polymethyl methacrylate (PMMA).

Research on the liquid-liquid two-phase flow of Newtonian fluids is prolific, with the flow pattern providing critical insights into the boundaries between various flow patterns and their generative mechanisms. Experimental parameters (i.e. velocity and flow rate) [23, 24] and dimensionless numbers (i.e. Capillary number, Weber number, and Reynolds number) [25, 26] can be used to characterize these flow patterns, consequently delineating the boundaries with clarity. Many studies on the flow and mass-transfer mechanisms of two-phase flow in various microdevices explored the flow, shape, breakup, and coalescence of droplets, covered theoretical, experimental, and numerical approaches, recognized the flow

patterns under diverse conditions and scrutinized the factors influencing these patterns [27].

Non-Newtonian [28, 29]/Newtonian fluids two-phase flow represents an emerging focus within two-phase flow research fields. While non-Newtonian fluids find extensive applications across industries, including food [30], energy [31], and biology [32] sectors, however, their unique properties such as shear-thinning/shear-thickening [33], Weissenberg effect [34], and Tom's phenomenon [35] add complexity to related studies. To comprehend these properties, researchers have deployed rheological parameters like viscosity ratio [36], material relaxation time [37], density ratio [38], and linked microchannel dimensions, dimensionless numbers, flow rate ratio with experimental phenomena such as droplet size, frequency, and flow patterns. Fu et al. [36] explored the flow patterns for cyclohexane-CMC two-phase flow in T-shaped rectangular microchannels, found that slug, droplet, parallel, and jet flow are the main flow patterns, studied the influence of the aspect ratio of microchannels and the mass fraction of solution on flow patterns, and plotted the flow pattern diagram. Venu et al. [37] investigated the flow patterns for oil-xanthan solution two-phase flow in a T-shaped microfluidic device, utilized the Carreau-Yasuda model to describe shear-thinning behavior of a non-Newtonian fluid, found that PF, DC, DTJ flow patterns occurred, and included the Carreau number to plot the flow pattern map. Vagner et al. [39] employed numerical modeling to analyze droplet characteristics of non-Newtonian/Newtonian fluids two-phase flow in coaxial microchannels, found a reduction in calculated droplet size with increased capillary flow speed ratio. Moreover, the droplet size showed a weak dependency on the velocity ratio of the continuous and dispersed phase. Taassob et al. [40] studied oil-xanthan solution flow patterns in a co-flow device, found that dripping and jetting flow patterns occurred, and examined the impact of dispersed phase viscosity and

 wng\_zh@i.shu.edu.cn (Z.L. Wang)

ORCID(s): 0000-0002-8382-4800 (Z.L. Wang)

Nomenclature			
$D$	Channel diameter ( $\mu\text{m}$ )	$\eta$	Apparent viscosity ( $\text{Pa} \cdot \text{s}$ )
$n$	Non-Newtonian index	$\eta_0$	Zero-shear-rate viscosity ( $\text{Pa} \cdot \text{s}$ )
$\lambda$	Material relaxation time (s)	$\eta_\infty$	Infinity-shear-rate viscosity ( $\text{Pa} \cdot \text{s}$ )
$Q$	Flow rate (ml/h)	Dimensionless numbers	
$u$	Velocity (m/s)	$Ca$	Capillary number
$f$	Droplet frequency ( $\text{s}^{-1}$ )	$We$	Weber number
$d^*$	Droplet equivalent diameter ( $\mu\text{m}$ )	$Re$	Reynolds number
	Greek symbols		Subscript
$\rho$	Density ( $\text{kg}/\text{m}^3$ )	1	Newtonian fluid
$\sigma$	Interfacial tension (N/m)	2	Non-Newtonian fluid
$\tau$	Capillary time (s)	$d$	Dispersed phase
$\dot{\gamma}$	Shear rate ( $\text{s}^{-1}$ )	$c$	Continuous phase

continuous phase speed on droplet formation. Khater et al. [41] examined the influence of the Capillary number, flow rate ratio, and agar mass fraction on light mineral oil-agar two-phase flow droplet formation in a flow-focusing microfluidic device, and their results suggested a decrease in droplet diameter with increasing agar mass fraction, and highlighted the Capillary number and flow speed ratio as primary factors in droplet volume and formation. Bai et al. [42] conducted a three-dimensional computational study of Janus droplet formation in a double Y-type microfluidic device, identified five different states of tubing, jetting, intermediate, dripping, and unstable dripping flow pattern under various flow conditions and noted the correlation between inlet flow speed and droplet size under low Capillary number conditions. Battat et al. [43] reviewed the generation of bubbles and droplets under varied Capillary number conditions across different microfluidic devices. Despite the diversity and complexity of non-Newtonian fluid two-phase flow, most research concentrates on power-law fluids [44] rather than Carreau fluids and predominantly uses cross-flow structures in microchannels. The flow pattern boundaries are generally the function of non-Newtonian fluid mass fraction, however, the correlations between flow patterns, droplet temporal and spatial characteristics, and non-Newtonian index  $n$ , and changes in solution mass fraction are seldom considered. Notably, no comparative studies on phase interchanging experiments have been reported.

Numerous studies, characterized by “front-end stretching and rear-end squeezing” mechanism, on two-phase flow in converging microchannels were conducted, and the unified temporal and spatial operation formula for all periodic monodisperse droplet (slug, dripping, and jetting) generation presented an outcome in microfluidics, thereby providing superior control capabilities [19, 20, 25]. This study investigates the temporal and spatial characteristics and flow patterns forming by monodisperse microdroplets, focuses on two-phase phase interchanging experiments involving non-Newtonian (NaAlg) and Newtonian (soybean oil) fluids in the convergent coaxial microchannel. Firstly, the Carreau model is modified and the relationship between the non-Newtonian index  $n$  and the mass fraction of NaAlg solution is studied. Subsequently, the dimensionless droplet frequency  $f \cdot \tau$  and dimensionless equivalent diameter  $d^*/D_c$  are introduced, and

$f \cdot \tau \sim (Q_d/Q_c)^n$  and  $d^*/D_c \sim (Q_d/Q_c)^n$  phase diagrams are plotted. Lastly, a synchronous transition phenomenon, where the interchanging of disperse and continuous phases will not affect their temporal and spatial characteristics of drop generating, is identified.

## 2. Materials and experimental setups

The experimental setups for non-Newtonian/Newtonian fluids two-phase flow, shown in Fig. 1, include three main sections: power, microchannel, and observation. The power section includes two peristaltic pumps (AP-0010, SP-6015, Sanotac). The microchannel section incorporates an inner needle (dispersed phase channel), an outer capillary glass tube (continuous phase channel), a PTFE tube, and a collector. The observation section integrates a supplementary light source, ground glass, a high-speed camera (Phantom V611-16G-M, Ametek) with a micro-lens (AT-X M100 PRO D, Tokina), and a computer system. The frame rate for the high-speed camera is 3000 fps and the experimental temperature is 25 °C.

The size of the microchannel is shown in Fig. 1, the continuous phase channel diameter  $D_c = 600\mu\text{m}$ , dispersed phase channel diameter  $D_d = 420\mu\text{m}$ , convergence angle  $\alpha = 8^\circ$ , and nozzle injection length  $X = 4000\mu\text{m}$ . During the experimentation process, the liquid of the continuous phase (phase  $c$ ) is first injected into the outer capillary glass tube by the peristaltic pump, and this process continues until the liquid saturates the outer capillary glass tube and achieves stability. Subsequently, the liquid of the dispersed phase is injected into the inner needle of the microchannel. Adjust the experimental parameters to achieve a steady observation by holding the dispersed phase flow rate  $Q_d$  and changing the continuous phase flow rate  $Q_c$ , then use the high-speed camera to capture images of the two-phase flow.

Detailed specifications of the experimental design are depicted in Table 1. The soybean oil (CP2015, Jinxiangyaofu) is used as the Newtonian fluids and various mass fractions (0.1 wt%, 0.5 wt%, 0.55 wt%, 1.0 wt%, 1.5 wt%) of NaAlg solution (S11053, Shyuanye) are used as the non-Newtonian fluid. Two distinctive experiments were established, with an interchanging of the dispersed and continuous phases: In Experiment A, the NaAlg solution serves as the dispersed phase and oil functions as the continuous phase, the flow rate of the dispersed phase  $Q_d$  ranges from 1 to 10 ml/h, and the

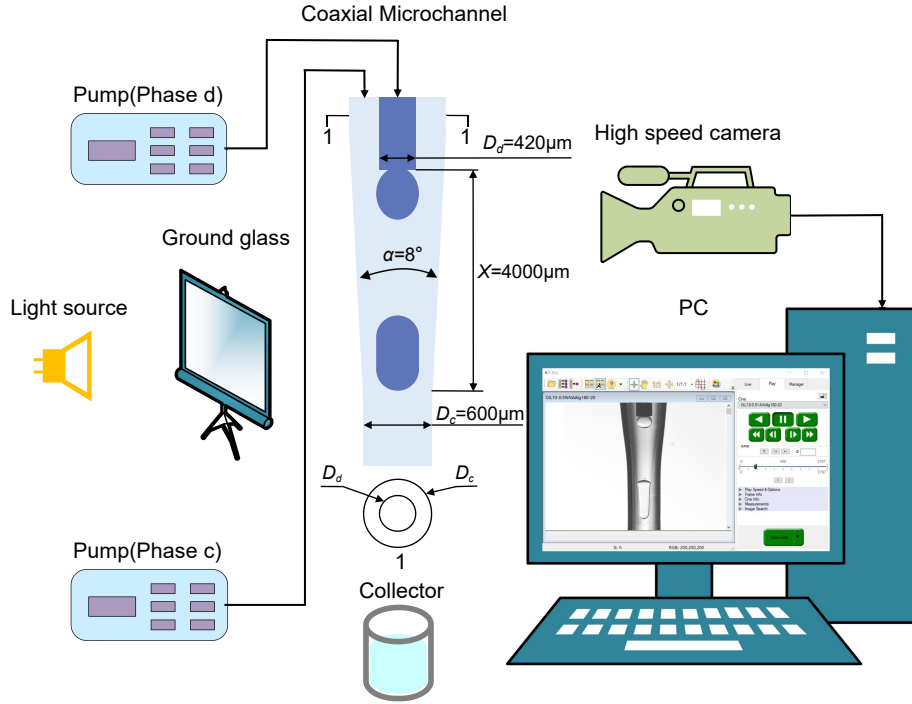


Fig. 1: The schematic microfluidic device.

flow rate of the continuous phase  $Q_c$  from 10 to 480 ml/h; In Experiment B, oil is designated as the dispersed phase and the NaAlg solution as the continuous phase, the flow rate of the dispersed phase  $Q_d$  ranges still from 1 to 10 ml/h, and the flow rate of the continuous phase  $Q_c$  from 1 to 250 ml/h.

Images of flow patterns are shown in Table 1. Slug, dripping, and jetting flow patterns, forming monodisperse microdroplets, were observed in the experiments. The slug flow pattern droplets are large and piston-like, the droplet vertical length  $l$  at the non-convergent downstream area is larger than or nearly the same as the diameter of the continuous phase microchannel  $D_c$ , and the boundaries make contact with the channel walls leading to blockages. The dripping flow pattern droplets are spherical or ellipsoidal, the droplet vertical length  $l$  at the non-convergent downstream area is either less than or approximate to the diameter of the continuous phase microchannel  $D_c$ . The jetting flow resembles the dripping flow, the droplet vertical length  $l$  at the non-convergent downstream area is obviously less than the diameter of the continuous phase microchannel  $D_c$ , and the dispersed phase fluid elongates at the inlet.

The detailed material properties are shown in Table 2. The NaAlg solution is prepared as follows: Initially, position a beaker on the electronic balance (JA302, Puchun), add specified quantities of NaAlg powders and deionized water. Subsequently, place the beaker on magnetic stirrer (ZGCJ-3A, Zigui) operating at the speed of 2500 r/min. Finally, once the NaAlg powder is fully dissolved, cease the stirring and wait for 24 h, ensuring complete degasification. Measure the solution's density. Measure the interfacial tension of the

NaAlg solution by tensiometer (CV-ZL1021, Cvok) and the shear viscosity of oil by viscometer (NDJ-5S, Lichen).

Phenomenological constitutive equations used to represent the rheological behavior of the non-Newtonian fluids are the Carreau model [45], the Power-Law model [46], the Cross model [47], and the Herschel-Bulkley model [48] and so on. The Carreau model, accounting for both shear-thinning and shear-thickening behaviors, aptly describes the consistent viscosity limits at low shear rates (zero-shear-rate viscosity  $\eta_0$ ) and high shear rates (infinity-shear-rate viscosity  $\eta_\infty$ ) [29]. The Carreau model is

$$\eta = (1 + (\lambda\dot{\gamma})^2)^{\frac{n-1}{2}} (\eta_0 - \eta_\infty) + \eta_\infty \quad (1)$$

where  $\eta$  is the apparent viscosity,  $\lambda$  is the material relaxation time,  $\dot{\gamma}$  is the shear rate and  $n$  is the non-Newtonian index. Then the viscosity limits are

$$\eta(\dot{\gamma} \rightarrow 0) \rightarrow \eta_0, \eta(\dot{\gamma} \rightarrow \infty) \rightarrow \eta_\infty \quad (2)$$

Rotational rheometer measurement data and the Carreau model fitting results are shown in Fig. 2. The calculation for the Carreau model parameters is as follows: Initially, set the shear rate range of rotational rheometer (MCR92, Anton Paar) from 0.1 to 200  $s^{-1}$  and measure the apparent viscosity  $\eta$  of the NaAlg solution under various shear rates  $\dot{\gamma}$ . Secondly, fit the data to a polynomial exponential function, compute the limit values at both zero and infinity shear rates  $\dot{\gamma}$ , and then estimate the zero-shear-rate viscosity  $\eta_0$  and infinity-shear-rate viscosity  $\eta_\infty$  for different mass fraction of the

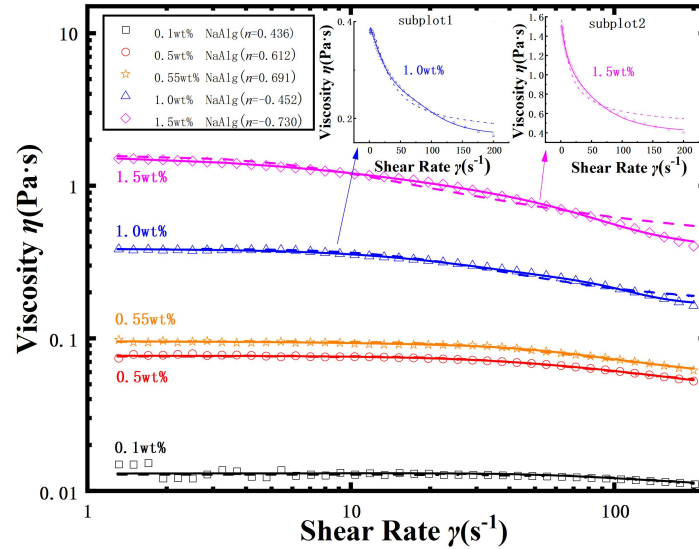
**Table 1**

The experimental design and flow pattern images.

Experiment	A	B
Flow rates	10 ml/h ≤ $Q_c$ ≤ 480 ml/h 1 ml/h ≤ $Q_d$ ≤ 10 ml/h	1 ml/h ≤ $Q_c$ ≤ 250 ml/h 1 ml/h ≤ $Q_d$ ≤ 10 ml/h
Phase $c$	Oil (Newtonian fluid-1)	NaAlg solution (non-Newtonian fluid-2)
Phase $d$	NaAlg solution (non-Newtonian fluid-2)	Oil (Newtonian fluid-1)

Image	Flow pattern	Slug	Dripping	Jetting	Slug	Dripping	Jetting



**Fig. 2:** Rotational rheometer measurement data for NaAlg solutions. NaAlg solution mass fractions used were 0.1 wt% (□), 0.5 wt% (○), 0.55 wt% (☆), 1.0 wt% (△), and 1.5 wt% (◇). Characterization results derived from the Carreau model and the modified Carreau model are depicted by dashed and solid lines respectively. Subplot 1 and Subplot 2 offer magnified views of the fitting results for 1.0 wt% and 1.5 wt% NaAlg solutions respectively.

NaAlg solution, which are shown in Table 2. Subsequently, use the multiple regression method to calculate the material relaxation time  $\lambda$  and non-Newtonian index  $n$  by rheological data.

As shown in Fig. 2, the apparent viscosity  $\eta$  escalates as the mass fraction increases. The subplots highlight that when the mass fraction is large (1.0 wt%, 1.5 wt%) and the corresponding viscosity  $\eta$  is high, the Carreau model exhibits considerable deviations as the shear rate  $\dot{\gamma}$  nears infinity, particularly when the mass fraction is larger, and the deviation is greater. To enhance the fitting accuracy, modify the Carreau model, which can be expressed as

$$\eta = (1 + \lambda_1 \dot{\gamma} + (\lambda_2 \dot{\gamma})^2 + (\lambda_3 \dot{\gamma})^3 + (\lambda_4 \dot{\gamma})^4)^{\frac{n-1}{2}} (\eta_0 - \eta_\infty) + \eta_\infty \quad (3)$$

where  $\lambda_1, \lambda_2, \lambda_3, \lambda_4$  are the polynomial material relaxation time.

Parameters of the modified Carreau model ( $\lambda_1, \lambda_2, \lambda_3, \lambda_4, n$ ) are shown in Table 2. Normally, Newtonian fluids are denoted as  $n = 1$ , and shear-thickening non-Newtonian fluids as  $n > 1$  [49], shear-thinning non-Newtonian fluids as  $0 < n < 1$  [50], with scarce literature documenting  $n < 0$

**Table 2**

Materials physical properties and Carreau model parameters.

Fluid	$\rho(\text{kg/m}^3)$	$\sigma(\text{N/m})$	$\eta_0(\text{Pa} \cdot \text{s})$	$\eta_\infty(\text{Pa} \cdot \text{s})$	$\lambda_1(\text{s})$	$\lambda_2(\text{s})$	$\lambda_3(\text{s})$	$\lambda_4(\text{s})$	$n$
Oil	929	-	0.063	0.063	-	-	-	-	1
0.1 wt%NaAlg	1001	0.058	0.013	0.010	-0.015	0.027	-0.018	0.013	0.436
0.5 wt%NaAlg	989	0.058	0.077	0.035	0.010	0.026	0	-0.013	0.612
0.55 wt%NaAlg	1023	0.054	0.096	0.044	0.045	-0.001	0	0.025	0.691
1.0 wt%NaAlg	1021	0.052	0.388	0.164	0.014	-0.035	-0.027	0.019	-0.452
1.5 wt%NaAlg	1081	0.065	1.582	0.388	0.049	0.016	0	0	-0.730

[51]. As shown in Fig. 2, the apparent viscosity  $\eta$  decreases with an increasing shear rate  $\dot{\gamma}$ , and the non-Newtonian index  $n < 1$ , which indicate that the NaAlg solutions are shear-thinning non-Newtonian fluids, and additionally, the non-Newtonian index  $n$  shifts from positive to negative as the mass fraction increases.

### 3. Results and discussion

#### 3.1. Limitations of traditional methods on phase diagrams for temporal and spatial behaviors

The frequency and size of droplets are the key parameters to study the droplet temporal and spatial characteristics. Dimensionless droplet frequency  $f \cdot \tau$  is frequently used by scholars to study the temporal characteristics of droplets [52]. The instances of the first  $t_1$  and  $i$ -th  $t_i$  droplets passing through a fixed position in the microchannel are recorded to calculate the droplet frequency  $f = \frac{i-1}{t_i-t_1}$ . The capillary time  $\tau = \sqrt{\rho_c D_c^3 / \sigma}$  refers to the time required for surface tension to influence dispersed phase droplets [53]. Given that the dimension of frequency  $f$  is the inverse of time ( $T^{-1}$ ), multiply it by  $\tau(T)$  for non-dimensionalization, and consequently, the definition of dimensionless frequency  $f \cdot \tau$  is

$$f \cdot \tau = f \cdot \sqrt{\frac{\rho_c D_c^3}{\sigma}} \quad (4)$$

Due to the inaccuracies in measuring the length of droplets, which arise from the convergent structure of the microchannel, droplets are modeled as spheres of equivalent volume, and consequently, the droplet volume  $V = Q_d / f$  can be represented by the sphere's radius  $r$  as  $V = 4\pi r^3 / 3$ . The sphere's diameter is regarded as the dispersed phase equivalent droplet diameter  $d^* = 2\sqrt[3]{3Q_d / 4\pi f}$ . The droplet equivalent diameter  $d^*$  is divided by the continuous phase microchannel diameter  $D_c$  to be dimensionless, and accordingly, the droplet dimensionless equivalent diameter is defined as

$$d^* / D_c = \sqrt[3]{\frac{6Q_d}{\pi f}} / D_c \quad (5)$$

Newtonian/Newtonian fluids two-phase flow commonly uses parameters such as velocity, flow rate, or dimensionless

numbers to delineate flow regimes. Wang et al. [20] established the convergence angle  $\alpha$  and needle displacement  $x$ , created diagrams illustrating four various flow regimes (slug, dripping, thin jet, saugage) at different dispersed phase flow rates  $Q_d$ , discovered that the boundaries shift in response to changes in needle displacement  $x$ , and used the continuous phase Capillary number  $Ca_c$  and the dispersed phase Weber number  $We_d$  to analyze the transition between Pan-dripping and Pan-jetting regions. Nevertheless, the inherent complexities of non-Newtonian fluids render conventional analysis methods more challenging. Bai et al. [42] plotted flow regime maps with the Capillary numbers of both the continuous  $Ca_c$  and dispersed phases  $Ca_d$ . Fu et al. [36] used the superficial velocity of the continuous  $u_c$  and dispersed phases  $u_d$  to create flow regime maps, revealing that changes in the mass fraction of CMC aqueous solutions influence the boundaries of flow regimes. The frequency and diameter of the droplets are often non-dimensionalized to study the relationship among droplet frequency, size, and flow regime. Taassob et al. [40] explored the relationship between the droplet dimensionless radius and various velocity ratios  $u_c / u_d$ , uncovering a jumping transition zone between dripping to jetting regimes. As shown in Fig. 3, the relationship between droplet frequency, droplet size, flow rate, and flow regime is studied by drawing  $f \cdot \tau \sim Q_d / Q_c$  and  $d^* / D_c \sim Q_d / Q_c$  phase diagrams for different mass fractions of NaAlg solutions based on conventional research methods.

As shown in Fig. 3, the study becomes complex after introducing the droplet dimensionless frequency  $f \cdot \tau$  and dimensionless equivalent diameter  $d^* / D_c$  because of the fluctuates of mass fractions. In order to tackle this challenge, key parameters of non-Newtonian fluids were introduced, including viscosity ratio  $\eta_c / \eta_d$ , material relaxation time  $\lambda$ , non-Newtonian index  $n$ , density ratio  $\rho_c / \rho_d$  and so on, which led to the critical realization that the non-Newtonian index  $n$  significantly influences the temporal and spatial analysis of droplets. Consequently, the non-Newtonian index  $n$  was integrated into the study to further examine the temporal and spatial characteristics of droplets.

#### 3.2. Significance of the non-Newtonian index $n$ in distributing temporal and spatial behaviors

##### 3.2.1. "Butterfly" in $f \cdot \tau \sim (Q_d / Q_c)^n$ phase diagrams

In order to study the distribution and transformation trends of flow regimes more effectively, employ the non-Newtonian index  $n$ , as shown in Fig. 4, and plot  $f \cdot \tau \sim$

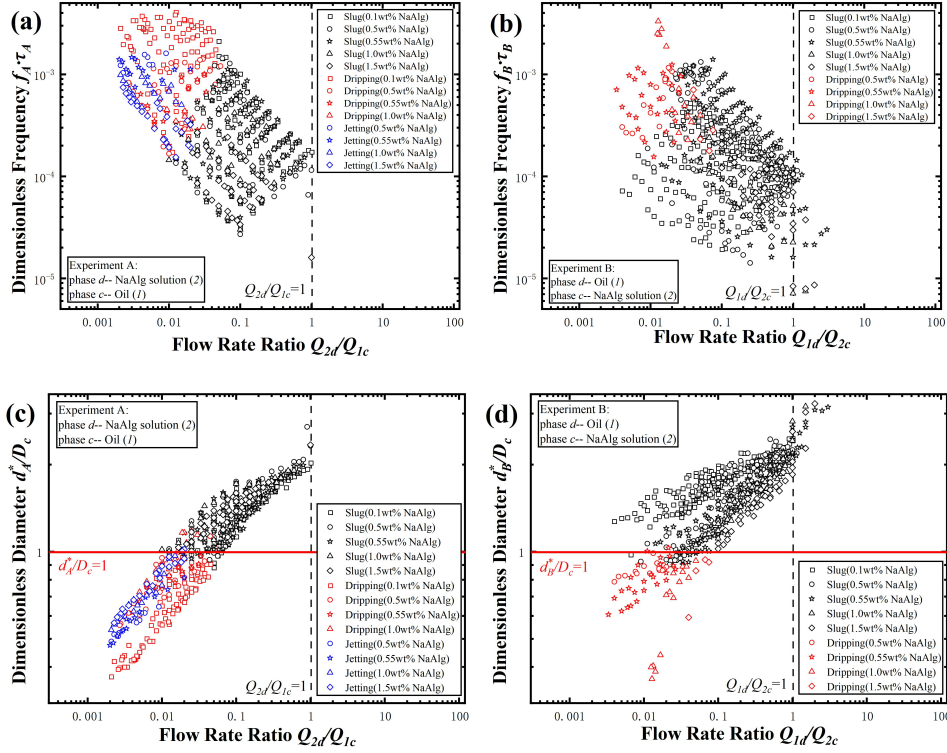


**Fig. 3:**  $f \cdot \tau \sim Q_d/Q_c$  and  $d^*/D_c \sim Q_d/Q_c$  phase diagrams for different mass fractions NaAlg solutions in two-phase interchanging experiments. NaAlg solution mass fractions used were 0.1 wt% ( $\square$ ), 0.5 wt% ( $\circ$ ), 0.55 wt% ( $\star$ ), 1.0 wt% ( $\triangle$ ), and 1.5 wt% ( $\diamond$ ). Slug (black), dripping (red), and jetting (blue) flow patterns were observed in the experiments. Dashed lines represent  $Q_d/Q_c = 1$  ( $Q_d = Q_c$ ), and red solid lines represent  $d^*/D_c = 1$ , which is the boundary between slug and other flow regimes. (a)  $f_A \cdot \tau_A \sim Q_{2d}/Q_{1c}$  phase diagram. In Experiment A, NaAlg solution serves as the dispersed phase and oil as the continuous phase. (b)  $f_B \cdot \tau_B \sim Q_{1d}/Q_{2c}$  phase diagram. In Experiment B, oil serves as the dispersed phase and NaAlg solution as the continuous phase. (c)  $d_A^*/D_c \sim Q_{2d}/Q_{1c}$  phase diagram. In Experiment A, NaAlg solution is the dispersed phase and oil the continuous phase. (d)  $d_B^*/D_c \sim Q_{1d}/Q_{2c}$  phase diagram. In Experiment B, oil serves as the dispersed phase and NaAlg solution as the continuous phase.

$(Q_d/Q_c)^n$  phase diagrams for NaAlg solutions of different mass fractions.

Some mass fractions of the NaAlg solution fail to yield dripping or jetting flow, which are shown in Table 3. In Experiment A, the predominant slug flow has the lowest droplet frequency  $f$  (metaphorically represented as the butterfly's body), the dripping flow shows slightly higher frequency  $f$  than slug flow, while the jetting flow has the highest frequency  $f$  and the broadest distribution (symbolized as the butterfly's wingtips). In Experiment B, the distribution pattern of slug and dripping flow mirrors that in Experiment A, except for the absence of jetting flow. Compared to Experiment A, more slug flows are generated in Experiment B, implying that the production of oil droplets is more easier than that of NaAlg droplets, when the flow rates of both phases remain unchanged ( $Q_{cB} = Q_{cA}$ ,  $Q_{dB} = Q_{dA}$ ).

The range of  $(Q_d/Q_c)^n$  in Experiment A is broader than that in Experiment B (leads to larger butterfly wings), as shown in Table 3, because when flow rate ratio  $Q_d/Q_c$  is small enough, the jet flow without droplets is produced. This phenomenon indicates that a decline in apparent viscosity  $\eta$

coincides with an increase in shear rate  $\dot{\gamma}$  as the velocity of NaAlg solutions  $u$  escalates. The combined viscous force and surface tension of the oil sufficiently counteract the inertial force of the NaAlg solution, preventing the continuous phase from shearing the dispersed phase and, consequently, inhibiting droplet formation.

The frequency range of NaAlg droplets  $f_A$  in Experiment A surpasses the oil droplet frequency  $f_B$  range observed in Experiment B (indicating a higher butterfly position), as shown in Table 3. Considering the capillary time in both experiments are approximate ( $\tau_A = \tau_B$ ), the prominent difference in the droplet dimensionless frequency  $f_A \cdot \tau_A$  and  $f_B \cdot \tau_B$  is primarily attributed to the substantial deviation in frequency  $f_A$  and  $f_B$ , and when dimensionless frequency  $f \cdot \tau$  exhibits a larger value, it indicates that the NaAlg solution facilitates droplet formation easier.

The boundaries among slug, dripping, and jetting flow are clear, as shown in Fig. 4. The non-Newtonian index  $n$ , displaying both positive and negative values, causes the NaAlg solution to distribute the flow regimes on both sides of the symmetry axis  $(Q_d/Q_c)^n = 1$  (represented as the middle of

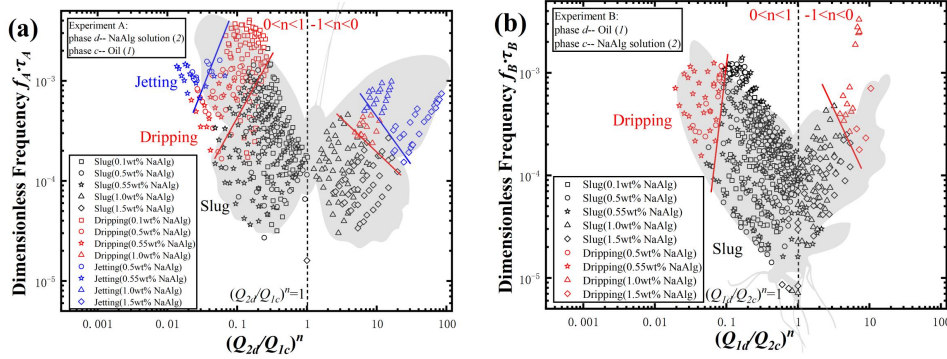


**Fig. 4:**  $f \cdot \tau \sim (Q_d/Q_c)^n$  phase diagrams for NaAlg solutions of different mass fractions in two-phase interchanging experiments. NaAlg solution mass fractions used were 0.1 wt% ( $\square$ ), 0.5 wt% ( $\circ$ ), 0.55 wt% ( $\star$ ), 1.0 wt% ( $\triangle$ ), and 1.5 wt% ( $\diamond$ ). Slug (black), dripping (red), and jetting (blue) flow patterns were observed in the experiments. Dashed lines represent  $(Q_d/Q_c)^n = 1$ , for either  $Q_d/Q_c = 1$  or  $n = 0$ , as the symmetry line for the flow regime distribution. (a) In Experiment A, NaAlg solution serves as the dispersed phase and oil as the continuous phase, the blue line demarcates the transition from jetting to dripping flow, whereas the red line defines the boundary between dripping and slug flow. (b) In Experiment B, oil serves as the dispersed phase and NaAlg solution as the continuous phase, and the red line delineates the boundary separating dripping and slug flow.

butterfly's body), and the respective flow regime distribution patterns are shown in Table 3. As the non-Newtonian index  $n$  converges to zero,  $(Q_d/Q_c)^n = 1$ , for either  $Q_d/Q_c = 1$  or  $n = 0$ , the flow regime distribution moves closer to the symmetry axis. However, in the experiments conducted, no non-Newtonian index with values of  $n = 0$  exhibited.

The study reveals that as the flow rate ratio  $Q_d/Q_c$  escalates, the droplet dimensionless frequency  $f \cdot \tau$  diminishes, indicating a flow regime shift favoring the genesis of large-scale droplets, which aligns with the results reported by Sontti et al. [52], as the non-Newtonian index  $n$  possesses both positive and negative values, and the changing patterns in the dimensionless frequency  $f \cdot \tau$  and flow regime are different, as shown in Table 3. Moreover, alterations in the solution mass fraction induce changes in the non-Newtonian index  $n$ , Sontti et al. [54] and Chen et al. [55] discerned that as power-law index of power-law fluids augments, there is a concurrent increase in apparent viscosity  $\eta$  and droplet frequency  $f$ , and a reduction in droplet volume, which subtly mirrored in the  $f \cdot \tau \sim (Q_d/Q_c)^n$  phase diagrams, but becomes more prominent in  $d^*/D_c \sim (Q_d/Q_c)^n$  phase diagrams in section 3.2.2. In addition, both Liu et al. [52] and Chen et al. [55] have proposed the use of the continuous phase Capillary number  $Ca_c$  to establish a scaling law between the droplet frequency  $f$  and the flow rate ratio  $Q_d/Q_c$ , proffering a promising avenue for future investigation.

### 3.2.2. "Grape" in $d^*/D_c \sim (Q_d/Q_c)^n$ phase diagrams

Employ the non-Newtonian index  $n$ , as shown in Fig. 5, and plot  $d^*/D_c \sim (Q_d/Q_c)^n$  phase diagrams for NaAlg solutions of different mass fractions.

As shown in Fig. 5, the slug flow, distinguishable by its larger droplet equivalent diameters  $d^*$ , is predominant in Experiment A (represented at the upper section of the grape bunch). On the other hand, the dripping flow exhibits marginally smaller equivalent diameters  $d^*$ , while the jetting

flow features the smallest yet most widespread equivalent diameters  $d^*$  (denoted at the tail of the grape bunch). Experiment B maintains similar slug and dripping distribution patterns to those of Experiment A, except without jetting formation. There is a clear boundary  $d^*/D_c = 1$  between slug and dripping flow (dividing the grape bunch into two distinct sections), with the slug flow above, and the dripping and jetting flow below, which is in alignment with the defined categorization of flow regimes.

The equivalent diameter range of NaAlg droplets  $d^*_A$  in Experiment A is narrower than that of oil droplets  $d^*_B$  in Experiment B (suggesting a lower grape bunch position), as shown in Table 3, and concurrently, a higher frequency of NaAlg droplet  $f_A$  formation is observed in Experiment A. This relationship is expounded by Equation (5), which establishes an inverse proportionality between droplet frequency  $f$  and their equivalent diameter  $d^*/D_c$ .

The fitted curves of different mass fractions of NaAlg (each delineated as a metaphorical bunch of grapes), as shown in Fig. 5, converge at a point on the symmetry axis  $(Q_d/Q_c)^n = 1$  of the flow regime distribution (depicted as the base of the grape bunch). In Experiment B, particular flow regimes emerge above the convergence point (forming the root of the grape bunch), and these regimes manifest when NaAlg mass fraction is elevated (0.55 wt%, 1.0 wt%, 1.5 wt%) and the dispersed phase flow rate  $Q_{1d}$  surpasses the continuous phase flow rate  $Q_{2c}$ . This suggests that the inertial force of the oil struggles to counterbalance viscous force of NaAlg solution, resulting in oil undergoing shear from the high-viscosity NaAlg solution and generating droplets. Notably, this phenomenon is absent in Experiment A, indicating the increased difficulty of shearing a high-viscosity NaAlg solution when oil is the continuous phase. Experiment A provides clear differentiation among the fitted curves for distinct mass fractions, and conversely, Experiment B exhibits a trend towards convergence in its fitted curves

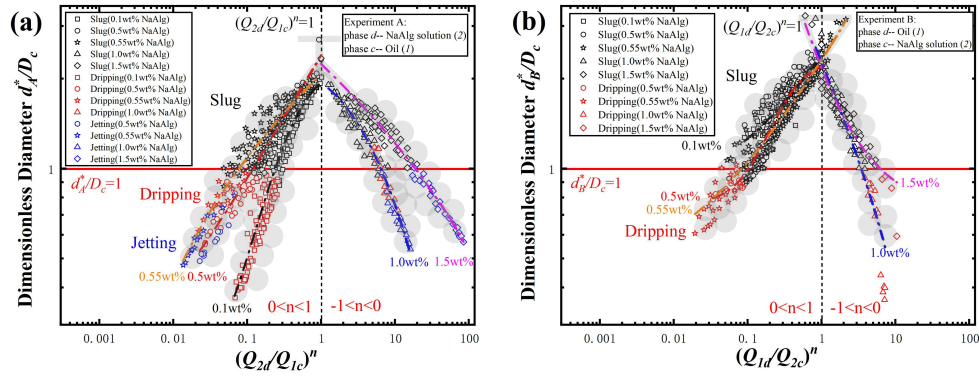


**Fig. 5:**  $d^*/D_c \sim (Q_d/Q_c)^n$  phase diagrams for NaAlG solutions of different mass fractions in two-phase interchanging experiments. NaAlG solution mass fractions used were 0.1 wt% ( $\square$ ), 0.5 wt% ( $\circ$ ), 0.55 wt% ( $\star$ ), 1.0 wt% ( $\triangle$ ), and 1.5 wt% ( $\diamond$ ). Slug (black), dripping (red), and jetting (blue) flow patterns were observed in the experiments. Dashed lines represent  $(Q_d/Q_c)^n = 1$ , for either  $Q_d/Q_c = 1$  or  $n = 0$ , as the symmetry line for the flow regime distribution, and red solid lines represent  $d^*/D_c = 1$ , which is the boundary between slug and other flow regimes. The distinct coloration of the dashed lines signifies the fitted curves associated with the flow regime distribution of varying NaAlG mass fraction. (a) In Experiment A, NaAlG solution serves as the dispersed phase and oil as the continuous phase. (b) In Experiment B, oil serves as the dispersed phase and NaAlG solution as the continuous phase.

(consolidating from four to two grape bunches), offering a compelling direction for subsequent research.

Experimental data indicate an augmentation in the dimensionless equivalent diameter  $d^*/D_c$  with an increasing flow rate ratio  $Q_d/Q_c$ , corroborating the results of previous studies by Fu et al. [12], Vagner et al. [39], Khater et al. [41], and Bai et al. [42]. This trend is attributable to the interplay between the shear stress imposed by the continuous phase fluid and the surface tension of the dispersed phase fluid, wherein an increase in the continuous phase flow rate  $Q_c$  leads to a higher pressure and velocity gradients at the surface, which results in augmented resistance, prompting the dispersed phase fluid to break down into smaller droplets. Conversely, a surge in the dispersed phase flow rate  $Q_d$  necessitates a greater energy accumulation by the continuous phase to fragment the dispersed phase, thereby facilitating the generation of larger droplets. Considering the non-Newtonian index  $n$  can possess both positive and negative values, the changing patterns in the dimensionless equivalent diameter  $d^*/D_c$  and flow regime are different, as shown in Table 3.

Changes in the mass fraction of the NaAlG solution alter the non-Newtonian index  $n$ . Findings from Experiment A revealed that, under equal flow rates of the two phases, an increased mass fraction of the NaAlG solution results in a higher apparent viscosity  $\eta$  and a larger dimensionless equivalent diameter  $d^*/D_c$ , which is similar to the influence of the power-law index on droplet size in power-law fluids observed by Sontti et al. [54], Chen et al. [55], and Agarwal et al. [37].

Fu et al. [12] noted an increase in droplet size corresponding to a reduction in the mass fraction of the PAAm solution. Vagner et al. [39] reported a decrease in droplet size associated with an increase in the continuous phase viscosity  $\eta_c$ . Furthermore, both Fu et al. [12] and Liu et al. [52] introduced the continuous phase Capillary number  $Ca_c$

to establish a scaling law between the dimensionless droplet size and flow rate ratio  $Q_d/Q_c$ , presenting a prospective direction for subsequent research.

### 3.3. Synchronous transition phenomenon of the temporal and spatial behaviors in two-phase interchanging experiments

Compare the droplet frequencies  $f$  and equivalent diameters  $d^*$  obtained from both Experiments A and B when the two-phase flow rates are identical ( $Q_c = Q_d$ ), as shown in Fig. 6.

As shown in Fig. 6, 0.55 wt% NaAlG solution marks the transition mass fraction threshold for synchronous transformations of temporal and spatial characteristics during phase interchanging experiments, and under this condition, the frequency  $f$  and equivalent diameters  $d^*$  of both NaAlG and oil droplets remain constant synchronously following the phase interchanging. The existence of this synchronous transition phenomenon is unrelated to the specific flow rate  $Q$ , but to the mass fraction of the NaAlG solutions. As shown in Table 4, compare the characteristics of NaAlG droplets in Experiment A with those of the oil droplets in Experiment B. Specifically, when the NaAlG solution mass fraction is lower, the frequency of NaAlG droplets is higher and the equivalent diameter of NaAlG droplets is smaller. Conversely, as the NaAlG solution mass fraction increases, the frequency diminishes and the equivalent diameter enlarges.

The Capillary number  $Ca$  signifies the ratio between shear stress and surface tension, the Weber number  $We$  encapsulates the ratio between inertia and surface tension, and the Reynolds number  $Re$  represents the ratio between inertial and viscous forces. The Carreau model, which is effective in characterizing low viscosity, is utilized in its primary definition for the computation of dimensionless numbers. In consideration of variations in velocity  $u$ , the

**Table 3**

The phenomena and patterns of the “butterfly distribution” and “grape distribution”.

Phenomena	Experiment A	Experiment B
Slug	Generated by all mass fractions	Generated by all mass fractions
Dripping	Generated except 1.5 wt%	Generated except 0.1 wt%
Jetting	Generated except 0.1 wt%	Not generated
$(Q_d/Q_c)^n$	0.01 ~ 85	0.02 ~ 10
$f \cdot \tau$	$3 \times 10^{-5} \sim 4 \times 10^{-3}$	$7 \times 10^{-6} \sim 3 \times 10^{-3}$
$d^*/D_c$	0.4 ~ 2.7	0.6 ~ 3.2
Flow pattern distribution	When $0 < n < 1$ , the distribution of flow is confined within $(Q_d/Q_c)^n < 1$ . When $-1 < n < 0$ , the distribution of flow is confined within $(Q_d/Q_c)^n > 1$ .	
$(Q_d/Q_c)^n$ increase	When $0 < n < 1$ , $f \cdot \tau$ reduces, $d^*/D_c$ augments, and dripping and jetting transfer to slug. When $-1 < n < 0$ , $f \cdot \tau$ augments, $d^*/D_c$ reduces, and slug transfers to dripping and jetting.	

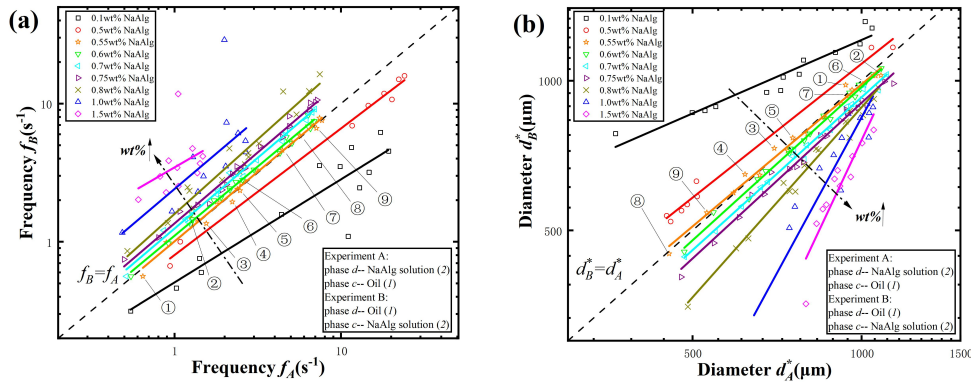


**Fig. 6:** Comparative graphs detailing the frequency  $f$  and equivalent diameter  $d^*$  of two-phase droplets in phase interchanging experiments with various mass fractions of NaAlg solution. NaAlg solution mass fractions used were 0.1 wt% (□), 0.5 wt% (○), 0.55 wt% (☆), 0.6 wt% (▽), 0.7 wt% (◁), 0.75 wt% (▷), 0.8 wt% (×), 1.0 wt% (△), and 1.5 wt% (◇). The nine marked points, from ① to ⑨, correspond to the experimental data under diverse two-phase flow conditions. Incremental mass fractions of NaAlg solution are indicated by dotted lines, and differently colored lines denote the fitted data lines for each distinct mass fraction. In Experiment A, NaAlg solution serves as the dispersed phase and oil as the continuous phase. In contrast, oil serves as the dispersed phase and NaAlg solution as the continuous phase in Experiment B. (a) Comparative graph of the two-phase droplet frequency  $f$  in phase interchanging experiments, with the dashed line representing a state of equality in this frequency ( $f_B = f_A$ ). (b) Comparative graph of the two-phase droplet equivalent diameter  $d^*$  in phase interchanging experiments, with the dashed line illustrating a state of equality for the two-phase droplet equivalent diameter ( $d_B^* = d_A^*$ ).

dynamic viscosity  $\eta'$  for non-Newtonian fluids is calculated as

$$\eta' = \left( \left( 1 + \left( \frac{3n+1}{4n} \frac{8u_2}{D} \lambda \right)^2 \right)^{\frac{n-1}{2}} (\eta_0 - \eta_\infty) + \eta_\infty \right) \left( \frac{3n+1}{4n} \right) \quad (6)$$

The velocity  $u_2 = Q_2 / \pi (D_2/2)^2$  is derived from the flow rate  $Q_2$ . The formulas used to calculate the three prevalent dimensionless numbers for both Newtonian fluids and shear-thinning non-Newtonian fluids [27] is shown in Table 5.

**Table 4**

Comparison of the droplet frequency  $f$  and the equivalent diameter  $d^*$  during phase transition.

Mass fraction	Droplet frequency $f$	Droplet equivalent diameter $d^*$
0.1 ~ 0.5 wt%	$f_A > f_B$	$d_A^* < d_B^*$
0.55 wt%	$f_A = f_B$	$d_A^* = d_B^*$
0.6 ~ 1.5 wt%	$f_A < f_B$	$d_A^* > d_B^*$

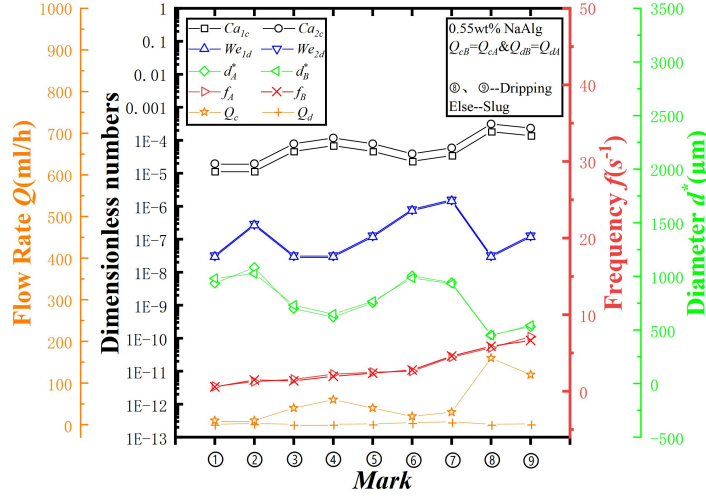
As shown in Fig. 7, various parameters derived from the nine two-phase flow conditions (shown in Fig. 6) for the 0.55 wt% NaAlg solution are included, such as flow rates of two phases, the Capillary number for the continuous phase  $Ca_c$ , the Weber number for the dispersed phase  $We_d$ , the droplet frequency  $f$ , and the equivalent diameter  $d^*$ .

Fig. 7 illustrates that the equivalent diameter  $d^*$  does not correspond with an increase in droplet frequency  $f$ , instead, its changing pattern mirrors the alterations of the dispersed phase Weber number  $We_d$ . The two phase flow rate

**Table 5**

The formulas for dimensionless numbers used in both Newtonian and non-Newtonian fluids.

Dimensionless numbers	Newtonian fluid	Non-Newtonian fluid
$Ca$	$Ca_1 = \frac{\eta_1 u_1}{\sigma}$	$Ca_2 = \frac{((1+(\frac{3n+1}{4n} \frac{8u_2}{D} \lambda)^2)^{\frac{n-1}{2}} (\eta_0 - \eta_\infty) + \eta_\infty)(\frac{3n+1}{4n}) u_2}{\sigma}$
$We$	$We_1 = \frac{\rho_1 D_1 u_1^2}{\sigma}$	$We_2 = \frac{\rho_2 D_2 u_2^2}{\sigma}$
$Re$	$Re_1 = \frac{\rho_1 D_1 u_1}{\eta_1}$	$Re_2 = \frac{\rho_2 D_2 u_2}{((1+(\frac{3n+1}{4n} \frac{8u_2}{D} \lambda)^2)^{\frac{n-1}{2}} (\eta_0 - \eta_\infty) + \eta_\infty)(\frac{3n+1}{4n})}$



**Fig. 7:** Comparative graph of experimental parameters in phase interchanging experiments using 0.55 wt% NaAlg solution with identical two phase flow rates ( $Q_{cB} = Q_{cA}$ ,  $Q_{dB} = Q_{dA}$ ). Nine sets of data denoted by markings ① to ⑨ is comprised. Notably, marks ⑧ and ⑨ generate dripping flow, while the remaining marks result in slug flow. The depicted parameters include the Capillary number of the continuous phase ( $Ca_{1c}$  ( $\square$ ),  $Ca_{2c}$  ( $\circ$ )), the Weber number of the dispersed phase ( $We_{1d}$  ( $\triangle$ ),  $We_{2d}$  ( $\nabla$ )), the droplet equivalent diameter ( $d_A^*$  ( $\diamond$ ),  $d_B^*$  ( $\triangleleft$ )), the droplet frequency ( $f_A$  ( $\triangleright$ ),  $f_B$  ( $\times$ )), and the two phase flow rate ( $Q_c$  ( $\star$ ),  $Q_d$  ( $+$ )).

remains consistent ( $Q_{cB} = Q_{cA}$ ,  $Q_{dB} = Q_{dA}$ ), which leads to minimal differences in two-phase droplet frequency  $f_A$  and  $f_B$  and equivalent diameters  $d_A^*$  and  $d_B^*$ , thereby maintaining the temporal and spatial characteristics of microdroplets synchronously constant. During instances of low Capillary number  $Ca$ , surface tension outstrips the shear stress, accounting for the insignificance of surface tension effects. The Weber number  $We$  is less than the Capillary number  $Ca$ , indicating a larger influence of velocity on the dimensionless numbers. When the flow rate of the dispersed phase  $Q_d$  is held constant, the increase of the continuous phase Capillary number  $Ca_c$  results in a decrease in the equivalent diameter  $d^*$ , which suggests that higher continuous phase Capillary number  $Ca_c$  results in greater shear stress, expediting the fragmentation process of the dispersed phase droplets and leading to the formation of smaller droplets [52]. Images and characteristic parameters of the droplets are shown in Table 6, when the 0.55 wt% NaAlg solution functions as the dispersed phase and the continuous phase respectively.

#### 4. Conclusions

In the present paper, the temporal and spatial behaviors of non-Newtonian and Newtonian fluids liquid-liquid system

with interchanging two phases in a converging coaxial microchannel has been studied. Two sets of experiments were conducted: Experiment A with NaAlg solution as the dispersed phase and soybean oil as the continuous phase, and Experiment B with soybean oil as the dispersed phase and NaAlg solution as the continuous phase. Three different flow patterns have been observed: slug, dripping, and jetting flow. Phase diagrams have been plotted in flow rate ratio  $Q_d/Q_c$ , the non-Newtonian index  $n$ , dimensionless droplet frequency  $f \cdot \tau$ , and dimensionless equivalent diameter  $d^*/D_c$ . The transition between the flow regimes has been found to be mainly described by  $n$ . Based on the results of this study, the following conclusions can be drawn:

(1) When NaAlg solution has high mass fractions (1.0 wt% and 1.5 wt%), the Carreau model exhibits some deviations. The Carreau model is modified to capture the shear-thinning behavior and the non-Newtonian index  $n$  is obtained. It is found that for higher viscosity, the non-Newtonian index can be  $n < 0$ , which is rarely reported, contributing to phase diagram separation and flow pattern classification.

(2)  $f \cdot \tau \sim Q_d/Q_c$  and  $d^*/D_c \sim Q_d/Q_c$  phase diagrams are plotted to verify the importance of  $n$ . Without

**Table 6**

Features of 0.55 wt% NaAlg droplets under identical two phase flow rates ( $Q_{cB} = Q_{cA}$ ,  $Q_{dB} = Q_{dA}$ ) in Experiments A and B.

Mark	①	②	③	④	⑤	⑥	⑦	⑧	⑨
$Q_d$ (ml/h)	1	3	1	1	2	5	7	1	2
$Q_c$ (ml/h)	10	10	40	60	40	20	30	160	120
Flow pattern	Slug	Slug	Slug	Slug	Slug	Slug	Slug	Dripping	Dripping
Image (Experiment A)									
Image (Experiment B)									

the introduction of  $n$ , boundaries between flow patterns are not clear, and temporal and spatial behaviors are difficult to analyze.

(3)  $f \cdot \tau \sim (Q_d/Q_c)^n$  and  $d^*/D_c \sim (Q_d/Q_c)^n$  phase diagrams are conducted by introducing  $n$ . In both Experiment A and Experiment B, clear boundaries between flow patterns are observed. The temporal behavior exhibits as a "butterfly distribution" and the spatial behavior as a "grape distribution". The distribution of flow patterns are divided by  $n$ , symmetric about  $(Q_d/Q_c)^n = 1$ , for either  $Q_d/Q_c = 1$  or  $n = 0$ . As for  $-1 < n < 0$ , an increase in  $(Q_d/Q_c)^n$  leads to an increase in  $f \cdot \tau$  and a decrease in  $d^*/D_c$ ; and as for  $0 < n < 1$ , the pattern is opposite.

(4) A synchronous transition phenomenon (0.55 wt% NaAlg solution) is identified when the two-phase flow rates remain constant ( $Q_{cB} = Q_{cA}$ ,  $Q_{dB} = Q_{dA}$ ) during phase interchanging. At this phenomenon shows, the temporal and spatial characteristics of microdroplets remain unchanged ( $f_A = f_B$ ,  $d_A^* = d_B^*$ ) after interchanging of disperse and continuous phases. As for lower mass fractions of NaAlg solution (0.1 wt%, 0.5 wt%),  $d_A^* \leq d_B^*$  and  $f_A \geq f_B$ ; and as for higher mass fractions (1.0 wt%, 1.5 wt%),  $d_A^* \geq d_B^*$  and  $f_A \leq f_B$ .

The modification of the Carreau model enables the non-Newtonian index  $n$  to have physical significance when it is negative. By conducting phase interchanging experiments in a converging coaxial microchannel, these findings are expected to provide better understanding on the temporal and spatial behaviors of non-Newtonian monodisperse microdroplets.

## Declaration of Competing Interest

The authors declare that they have no known competing financial interests or personal relationships that could have appeared to influence the work reported in this paper.

## Acknowledgements

The author acknowledges the Natural Science Foundation of China (No. 11832017 and 11772183).

## References

- [1] A. S. Lari, P. Zahedi, H. Ghourchian, A. Khatibi, Microfluidic-based synthesized carboxymethyl chitosan nanoparticles containing metformin for diabetes therapy: In vitro and in vivo assessments, *Carbohydrate Polymers* 261 (2021).
- [2] W. Su, D. Liang, M. Tan, Microfluidic strategies for sample separation and rapid detection of food allergens, *Trends in Food Science & Technology* 110 (2021) 213–225.
- [3] W. Tan, E. Powles, L. Zhang, W. Shen, Go with the capillary flow. simple thread-based microfluidics, *Sensors and Actuators B-Chemical* 334 (2021).
- [4] W.-Y. Huang, S.-T. Chou, C.-H. Chen, S.-Y. Chou, J.-H. Wu, Y.-C. Chen, G.-B. Lee, An automatic integrated microfluidic system for allergy microarray chips, *Analyst* 143 (2018) 2285–2292.
- [5] B. Zheng, L. S. Roach, R. F. Ismagilov, Screening of protein crystallization conditions on a microfluidic chip using nanoliter-size droplets, *Journal of the American Chemical Society* 125 (2003) 11170–11171.
- [6] L. H. Hung, K. M. Choi, W. Y. Tseng, Y. C. Tan, K. J. Shea, A. P. Lee, Alternating droplet generation and controlled dynamic droplet fusion in microfluidic device for cds nanoparticle synthesis, *Lab on a Chip* 6 (2006) 174–178.
- [7] L. Zhai, Z. Meng, J. Yang, H. Zhang, N. Jin, Detection of interfacial structures in inclined liquid-liquid flows using parallel-wire array probe and planar laser-induced fluorescence methods, *Sensors* 20 (2020).

- [8] J.-y. Qian, X.-j. Li, Z. Wu, Z.-j. Jin, B. Sundén, A comprehensive review on liquid-liquid two-phase flow in microchannel: flow pattern and mass transfer, *Microfluidics and Nanofluidics* 23 (2019).
- [9] Q. Xu, M. Hashimoto, T. T. Dang, T. Hoare, D. S. Kohane, G. M. Whitesides, R. Langer, D. G. Anderson, Preparation of monodisperse biodegradable polymer microparticles using a microfluidic flow-focusing device for controlled drug delivery, *Small* 5 (2009) 1575–1581.
- [10] L. B. Zhao, L. Pan, K. Zhang, S. S. Guo, W. Liu, Y. Wang, Y. Chen, X. Z. Zhao, H. L. W. Chan, Generation of janus alginate hydrogel particles with magnetic anisotropy for cell encapsulation, *Lab on a Chip* 9 (2009) 2981–2986.
- [11] B. Zheng, J. D. Tice, R. F. Ismagilov, Formation of arrayed droplets of soft lithography and two-phase fluid flow, and application in protein crystallization, *Advanced Materials* 16 (2004) 1365–1368.
- [12] T. Fu, Y. Ma, H. Z. Li, Breakup dynamics of slender droplet formation in shear-thinning fluids in flow-focusing devices, *Chemical Engineering Science* 144 (2016) 75–86.
- [13] A. V. Kovalev, A. A. Yagodnitsyna, A. V. Bilsky, Flow hydrodynamics of immiscible liquids with low viscosity ratio in a rectangular microchannel with t-junction, *Chemical Engineering Journal* 352 (2018) 120–132.
- [14] S. Timung, V. Tiwari, A. K. Singh, T. K. Mandal, D. Bandyopadhyay, Capillary force mediated flow patterns and non-monotonic pressure drop characteristics of oil-water microflows, *Canadian Journal of Chemical Engineering* 93 (2015) 1736–1743.
- [15] M. Dang, J. Yue, G. Chen, Q. Yuan, Formation characteristics of Taylor bubbles in a microchannel with a converging shape mixing junction, *Chemical Engineering Journal* 223 (2013) 99–109.
- [16] S. Yin, J. Pei, J. Peng, L. Zhang, C. Srinivasakannan, Study on mass transfer behavior of extracting Ia(iii) with ehepa (p507) using rectangular cross-section microchannel, *Hydrometallurgy* 175 (2018) 64–69.
- [17] S. G. Sontti, A. Atta, Formation characteristics of Taylor bubbles in power-law liquids flowing through a microfluidic co-flow device, *Journal of Industrial and Engineering Chemistry* 65 (2018) 82–94.
- [18] C. Deng, H. Wang, W. Huang, S. Cheng, Numerical and experimental study of oil-in-water (o/w) droplet formation in a co-flowing capillary device, *Colloids and Surfaces A-Physicochemical and Engineering Aspects* 533 (2017) 1–8.
- [19] Z. L. Wang, Speed up bubbling in a tapered co-flow geometry, *Chemical Engineering Journal* 263 (2015) 346–355.
- [20] Z. L. Wang, Universal self-scalings in a micro-co-flowing, *Chemical Engineering Science* 262 (2022).
- [21] P. Wu, Z. Luo, Z. Liu, Z. Li, C. Chen, L. Feng, L. He, Drag-induced breakup mechanism for droplet generation in dripping within flow focusing microfluidics, *Chinese Journal of Chemical Engineering* 23 (2015) 7–14.
- [22] X. Chen, C. L. Ren, Experimental study on droplet generation in flow focusing devices considering a stratified flow with viscosity contrast, *Chemical Engineering Science* 163 (2017) 1–10.
- [23] Q. Wang, X. Su, Y. Feng, H. Wang, J. Song, Experimental study of gas-water digital microflow patterns in fracture: Implication for enhancing coalbed methane production, *Journal of Petroleum Science and Engineering* 207 (2021).
- [24] S. Lee, J. Lee, Surface hydrophobicity change on adiabatic two-phase flow pattern transitions in horizontal tubes, *Experimental Thermal and Fluid Science* 120 (2021).
- [25] J. Zhang, C. Wang, X. Liu, C. Yi, Z. L. Wang, Experimental studies of microchannel tapering on droplet forming acceleration in liquid paraffin/ethanol coaxial flows, *Materials* 13 (2020).
- [26] R. K. Verma, S. Ghosh, Effect of phase properties on liquid-liquid two-phase flow patterns and pressure drop in serpentine mini geometry, *Chemical Engineering Journal* 397 (2020).
- [27] A. T. S. Cerdeira, J. B. L. M. Campos, J. M. Miranda, J. D. P. Araujo, Review on microbubbles and microdroplets flowing through microfluidic geometrical elements, *Micromachines* 11 (2020).
- [28] E. Lakzian, P. Akbarzadeh, Numerical investigation of unsteady pulsatile newtonian/non-newtonian blood flow through curved stenosed arteries, *Bio-Medical Materials and Engineering* 30 (2020) 525–540.
- [29] D. Picchi, I. Barmak, A. Ullmann, N. Brauner, Stability of stratified two-phase channel flows of newtonian/non-newtonian shear-thinning fluids, *International Journal of Multiphase Flow* 99 (2018) 111–131.
- [30] F. Xie, P. J. Halley, L. Averous, Rheology to understand and optimize processability, structures and properties of starch polymeric materials, *Progress in Polymer Science* 37 (2012) 595–623.
- [31] N. Schneider, M. Gerber, Rheological properties of digestate from agricultural biogas plants: An overview of measurement techniques and influencing factors, *Renewable & Sustainable Energy Reviews* 121 (2020).
- [32] C.-X. Zhao, A. P. J. Middelberg, Two-phase microfluidic flows, *Chemical Engineering Science* 66 (2011) 1394–1411.
- [33] F. J. Granados-Ortiz, M. Jimenez-Salas, J. Ortega-Casanova, Application of shear-thinning and shear-thickening fluids to computational fluid mechanics of high-reynolds impinging turbulent jets for cooling engineering, *International Journal of Thermal Sciences* 162 (2021).
- [34] Y. N. Huang, W. D. Su, C. B. Lee, On the weissenberg effect of turbulence, *Theoretical and Applied Mechanics Letters* 9 (2019) 236–245.
- [35] K. S. Sokhal, D. Gangacharyulu, V. K. Bulasara, Effect of guar gum and salt concentrations on drag reduction and shear degradation properties of turbulent flow of water in a pipe, *Carbohydrate Polymers* 181 (2018) 1017–1025.
- [36] T. Fu, L. Wei, C. Zhu, Y. Ma, Flow patterns of liquid-liquid two-phase flow in non-newtonian fluids in rectangular microchannels, *Chemical Engineering and Processing-Process Intensification* 91 (2015) 114–120.
- [37] V. G. Agarwal, R. Singh, S. S. Bahga, A. Gupta, Dynamics of droplet formation and flow regime transition in a t-shaped microfluidic device with a shear-thinning continuous phase, *Physical Review Fluids* 5 (2020).
- [38] M. Dziubinski, H. Fidos, M. Sosno, The flow pattern map of a two-phase non-newtonian liquid-gas flow in the vertical pipe, *International Journal of Multiphase Flow* 30 (2004) 551–563.
- [39] S. A. Vagner, S. A. Patlazhan, C. A. Serra, Iop, Formation of microdroplets in newtonian and shear thinning fluids flowing in coaxial capillaries: Numerical modeling, in: *32nd International Conference on Interaction of Intense Energy Fluxes with Matter (ELBRUS)*, volume 946 of *Journal of Physics Conference Series*, 2018, pp. 1–6. URL: <GotoISI>://WOS:000446782200117. doi:10.1088/1742-6596/946/1/012117.
- [40] A. Taassob, M. K. D. Manshadi, A. Bordbar, R. Kamali, Monodisperse non-newtonian micro-droplet generation in a co-flow device, *Journal of the Brazilian Society of Mechanical Sciences and Engineering* 39 (2017) 2013–2021.
- [41] A. Khater, O. Abdelrehim, M. Mohammadi, M. Azarmanesh, M. Jonmaleki, R. Salahandish, A. Mohamad, A. Sanati-Nezhad, Picoliter agar droplet breakup in microfluidics meets microbiology application: numerical and experimental approaches, *Lab on a Chip* 20 (2020) 2175–2187.
- [42] F. Bai, H. Zhang, X. Li, F. Li, S. W. Joo, Generation and dynamics of janus droplets in shear-thinning fluid flow in a double y-type microchannel, *Micromachines* 12 (2021).
- [43] S. Battat, D. A. Weitz, G. M. Whitesides, Nonlinear phenomena in microfluidics, *Chemical Reviews* 122 (2022) 6921–6937.
- [44] S. Kumar, V. Kumar, A. K. Singh, Influence of lubricants on the performance of journal bearings - a review, *Tribology-Materials Surfaces & Interfaces* 14 (2020) 67–78.
- [45] J. L. Kokini, K. L. Bistany, M. P. L., Predicting steady shear and dynamic viscoelastic properties of guar and carrageenan using the bird-carreau constitutive model, *Journal of Food Science* 49 (1984) 1569–1572.
- [46] A. Waele, Viscometry and plastometry, *Oil Colour Chemists' Assoc* 6 (1923) 33–88.

- [47] M. M. Cross, Rheology of non-newtonian fluids: a new flow equation for pseudoplastic systems, *Journal of Colloid Science* 20 (1965) 417–437.
- [48] W. H. Herschel, R. Bulkley, Konsistenzmessungen von gummi-benzollösungen, *Kolloid-Zeitschrift* 39 (1926) 291–300.
- [49] A. Dhiman, R. Ghosh, L. Baranyi, Hydrodynamic and thermal study of a trapezoidal cylinder placed in shear-thinning and shear-thickening non-newtonian liquid flows, *International Journal of Mechanical Sciences* 157 (2019) 304–319.
- [50] C. Airiau, A. Bottaro, Flow of shear-thinning fluids through porous media, *Advances in Water Resources* 143 (2020).
- [51] K. Suresh, R. V. Kumar, R. Boro, M. Kumar, G. Pugazhenti, Rheological behavior of polystyrene (ps)/co-al layered double hydroxide (ldh) blend solution obtained through solvent blending route: Influence of ldh loading and temperature, in: *International Conference on Processing of Materials, Minerals and Energy (PMME)*, volume 5, 2018, pp. 1359–1371. URL: <GotoISI>://WOS:000428718200178. doi:10.1016/j.matpr.2017.11.222.
- [52] C. Liu, Q. Zhang, C. Zhu, T. Fu, Y. Ma, H. Z. Li, Formation of droplet and "string of sausages" for water-ionic liquid (bmim pf6) two-phase flow in a flow-focusing device, *Chemical Engineering and Processing-Process Intensification* 125 (2018) 8–17.
- [53] W. Du, T. Fu, Y. Duan, C. Zhu, Y. Ma, H. Z. Li, Breakup dynamics for droplet formation in shear-thinning fluids in a flow-focusing device, *Chemical Engineering Science* 176 (2018) 66–76.
- [54] S. G. Sontti, A. Atta, Cfd analysis of microfluidic droplet formation in non-newtonian liquid, *Chemical Engineering Journal* 330 (2017) 245–261.
- [55] Q. Chen, J. Li, Y. Song, D. M. Christopher, X. Li, Modeling of newtonian droplet formation in power-law non-newtonian fluids in a flow-focusing device, *Heat and Mass Transfer* 56 (2020) 2711–2723.